Engineering Fracture Mechanics 308 (2024) 110325

Contents lists available at ScienceDirect

Engineering Fracture Mechanics

journal homepage: www.elsevier.com/locate/engfracmech

CDPM2F: A damage-plasticity approach for modelling the failure of strain hardening cementitious composites

Chao Zhou, Antoine Marlot, Peter Grassl *

James Watt School of Engineering, University of Glasgow, Glasgow, UK

ARTICLE INFO

Keywords:
Engineered cementitious composites
Fracture
Damage
Plasticity
Constitutive model

ABSTRACT

For the use of micro-mechanics based constitutive models for fibre reinforced strain hardening cementitious composites in finite element simulations of structural components, it is required to link the crack opening at the scale of fibres to the cracking strain at the scale of structural components. We aim to establish this link by incorporating a micro-mechanics based fibre bridging stress crack opening law into a macroscopic damage-plasticity approach, which we call CDPM2F. The model is implemented in the open-source finite element program OOFEM. The model produces mesh-insensitive results and its response agrees well with experimental results for failure in tension, shear and compression reported in the literature.

1. Introduction

Strain hardening cementitious composites (SHCC), studied for instance in [1–3], are fibre reinforced cementitious materials which exhibit significantly larger strains at maximum tensile stress than ordinary fibre reinforced concrete [4]. The hardening response is influenced by several properties, such as aspect ratio of fibres, the interface response between fibres and matrix, matrix strength, fibre stiffness and strength, as well as volume fraction of fibres used. One important property is the interface response between fibre and matrix, which leads to a fibre force versus crack opening curve, which exhibits hardening beyond the debonding stage. The mechanism responsible for this hardening response is the jamming of fibre material at the interface which is generated by the surface of the fibres being peeled off due to the slip between fibre and matrix [5]. If the fibre properties are chosen to provide strain hardening of the fibre reinforced composite [6], the hardening response in tension is characterised by multiple cracking of the matrix with very small crack spacing [5]. Once the tensile capacity of the fibre reinforced composite is reached the softening response is accompanied by localisation of distributed cracking into a single crack [7].

In certain types of SHCC, such as engineered cementitious composites (ECC), fibres with a high aspect ratio (e.g. greater than 200) and a fibre diameter of less than 50 μm are used [8]. Generating meshes for these thin fibres for finite element simulations of structural components is not feasible. As an example, in [9] a long specimen with a single steel reinforcement bar and ECC matrix was investigated. For this experiment, the centre length is 813 mm. The square cross-section has an edge length of 127 mm. The steel reinforcement bar has a diameter of 16 mm. Consequently, the matrix volume in the central part of the specimen is $813 \times 127 \times 127 - 813 \times \pi 16^2/4 = 12.9 \times 10^6\ \mathrm{mm}^3$. For the PVA fibres used, the fibre length is 12.7 mm and the fibre diameter is 0.04 mm, which results in the volume of a single fibre of $12.7 \times \pi \times 0.04^2/4 = 0.016\ \mathrm{mm}^3$. Therefore, for a fibre volume fraction of 0.02 as in the experiments the number of fibres is $0.02 \times 12.9 \times 10^6/0.016 = 16.2 \times 10^6$. Consequently, for analysing these type of structural specimens made of SHCC such as ECC, it is desired to develop macroscopic constitutive models which represent the average SHCC response based on fibre properties.

* Corresponding author.
E-mail address: peter.grassl@glasgow.ac.uk (P. Grassl).

https://doi.org/10.1016/j.engfracmech.2024.110325
Received 29 April 2024; Received in revised form 15 July 2024; Accepted 18 July 2024
Available online 2 August 2024

Fibre bridging constitutive laws developed in the literature are the basis for the development of these constitutive models. These laws relate the average tensile stress transmitted by randomly arranged fibres across a matrix crack to the crack opening. Bao and Song [10] proposed bond stress-slip models for general fibre reinforced composites. Lin and Li [11] developed a constitutive model of fibre bridging based on a bond stress-slip hardening relation which is focused on SHCC. This popular bridging law was further extended to consider two sided pullout in [12]. The results obtained with this extension are close to those obtained with the one sided pullout model. In [13], the fibre bridging law was further extended to consider fibre fracture.

These type of fibre bridging constitutive laws have been used successfully in macroscopic models [14–17]. In these models, a very fine finite element mesh is used to be able to describe the individual matrix cracks during the strain hardening process. Although these type of models are successful in simulating structural components, they are computationally intensive, because of the need of fine meshes to reproduce the crack spacing.

In another group of models, the individual fibre force versus crack opening relation is used efficiently in a rigid body spring model framework [18,19]. These models are useful to investigate detailed fracture processes of small components. However, since fibres are modelled explicitly, these modelling approaches have not been applied to larger structural components. In addition, the use of crack opening of the matrix relies on being able to model individual cracks during the hardening stage of SHCC.

The aim of this research is to develop a macroscopic constitutive model for SHCC in which the hardening response is described in the form of a stress strain law and which, at the same time, is based on a fibre bridging model in a way, so that the constitutive model can be used for general triaxial stress states. We aim to achieve this by combining the fibre bridging model developed in [11] with the concrete damage plasticity model CDPM2 reported in [20]. The expected advantage of the proposed modelling concept over existing models is that the hardening stage of the tensile response of SHCC is modelled using a stress–strain relation, which allows for the use of large element sizes, because the formation of individual cracks during the hardening stage is not modelled. The proposed techniques are developed for cementitious materials. However, it is believed that the concept applies to a wide range of short fibre reinforced composites. The model response is compared to experimental results for direct tensile, shear and compression tests made of SHCC. It is shown that the proposed modelling approach can reproduce the experiments well and produces results without pathological mesh dependence.

2. Concrete damage-plasticity model CDPM2F for SHCC

The present section describes CDPM2F, which is an extension of the concrete damage-plasticity model CDPM2 to SHCC proposed in this study. The original CDPM2 is a 3D concrete damage-plasticity model presented in [20], which has been shown to produce good results for a wide range of concrete fracture tests [21,22]. These tests include tensile, shear and compressive fracture processes of unconfined and confined concrete. Here, CDPM2 is extended to CDPM2F by combining it with a fibre bridging law proposed in [11].

CDPM2 is based on the concept of combining scalar damage with tensorial plasticity. The nominal stress $\boldsymbol{\sigma}$ is

$$\boldsymbol{\sigma} = \left(1 - \omega_{\mathrm{t}}\right) \bar{\boldsymbol{\sigma}}_{\mathrm{t}} + \left(1 - \omega_{\mathrm{c}}\right) \bar{\boldsymbol{\sigma}}_{\mathrm{c}} \tag{1}$$

Here, ω_{t} and ω_{c} are the tensile and compressive damage variables, respectively. Furthermore, $\bar{\boldsymbol{\sigma}}_{\mathrm{t}}$ and $\bar{\boldsymbol{\sigma}}_{\mathrm{c}}$ are the positive and negative parts of the effective stress $\bar{\boldsymbol{\sigma}}$, respectively. The two parts of the effective stress are determined from the principal components of the effective stress $\bar{\boldsymbol{\sigma}} = \mathbf{D}_{\mathrm{e}} \left(\boldsymbol{\varepsilon} - \boldsymbol{\varepsilon}_{\mathrm{p}}\right)$. Here, $\mathbf{D}_{\mathrm{e}}$ is the elastic stiffness, $\boldsymbol{\varepsilon}$ is the strain and $\boldsymbol{\varepsilon}_{\mathrm{p}}$ is the plastic strain. For a description of the equations of CDPM2, it is referred to [20], which contains all required details. Here we focus on the extension of CDPM2 to SHCC, for which we only adjust the tensile damage part of the model which is derived based on a 1D tensile response of the material of the form

$$\sigma = (1 - \omega_{\mathrm{t}})\bar{\sigma} = \left(1 - \omega_{\mathrm{t}}\right) E \left(\varepsilon - \varepsilon_{\mathrm{p}}\right) = E \left(\varepsilon - \varepsilon_{\mathrm{cr}}\right) \tag{2}$$

because in 1D tension $\bar{\sigma}_{\mathrm{t}} = \bar{\sigma} = E \left(\varepsilon - \varepsilon_{\mathrm{p}}\right)$. In (2), the inelastic strain component $\varepsilon_{\mathrm{cr}}$ is defined as

$$\varepsilon_{\mathrm{cr}} = \varepsilon_{\mathrm{p}} + \omega_{\mathrm{t}} \left(\varepsilon - \varepsilon_{\mathrm{p}}\right) \tag{3}$$

where ε_{p} is the irreversible and $\omega_t \left(\varepsilon - \varepsilon_p\right)$ is the reversible inelastic strain part. The damage variable ω_{t} is in the range from 0 (undamaged) to 1 (fully damaged). The composition of the two parts of the inelastic strain are controlled by the hardening modulus H_{p} of the plasticity part of CDPM2 [20], which determines the effective stress of the undamaged material. The damage variable ω_{t} is then used to reduce the effective stress to obtain the nominal stress. For $H_{\mathrm{p}} = 0$, the majority of the cracking strain is composed of the irreversible part, because the plasticity part does not exhibit any hardening and damage is only used to reduce the stress from the level of the tensile strength during the softening response. For $H_p \rightarrow 1$, the plastic strain approaches zero and the cracking strain is mainly reversible.

For SHCC, the 1D stress–strain law in (2) is the sum of stresses transmitted in the matrix and by the fibres as

$$\sigma = E \left(\varepsilon - \varepsilon_{\mathrm{cr}}\right) = \sigma_{\mathrm{m}}(\delta) + \sigma_{\mathrm{f}}(\delta) \tag{4}$$

where σ_{m} is the matrix and σ_{f} is the fibre stress in direct tension and δ is the crack opening. For the fibre stress, we propose a new model described in Section 3. For the concrete stress, we use an exponential stress crack opening curve of the form

$$\sigma_{\mathrm{m}} \left(\delta\right) = f_{\mathrm{t}} \exp\left(-\frac{\delta}{\delta_{\mathrm{f}}}\right) \tag{5}$$

Here, f_t is the tensile strength of the matrix and δ_f is the crack open threshold which controls the softening slope. Since the damage-plasticity model is a function of the cracking strain ϵ_{cr} and the matrix and fibre models are functions of the crack opening δ, a link between crack opening and cracking strain is required which will be introduced in Section 4. With this link, both cracking strain in (3) and crack opening are functions of the damage variable ω_t, which is determined iteratively from (4).

3. Fibre bridging stress versus crack opening

In this section, the model for the fibre stress versus crack opening $\sigma_f(\delta)$ in (4) is derived. The model is an adjustment of the approach presented in [11] to make it suitable for the iterative solution process used in this study. First, we will summarise the original approach in [11] and then present our modification.

3.1. Original model by Lin and Li (1997)

We present here in compact form the equations reported in [11] so that readers can follow the modification of the model, which was then used in the continuum based damage-plasticity approach CDPM2.

In [11], the pullout force P of a single fibre crossing a single crack is given as a function of the crack opening δ as

$$P(\delta) = \begin{cases} \dfrac{\pi d_f^2 \tau_0 (1+\eta)}{\omega} \sqrt{\left(1 + \dfrac{c\delta}{L_f}\right)^2 - 1} & \text{if } 0 \le \delta \le \delta_0 \\ \dfrac{\pi d_f^2 \tau_0 (1+\eta)}{\omega} \left[\sinh\left(\omega \dfrac{L}{d_f}\right) - \sinh\left(\dfrac{\omega(\delta-\delta_0)}{d_f}\right)\right] & \text{if } \delta_0 \le \delta \le L \\ +\ \pi \tau_0 \beta (1+\eta)(\delta - \delta_0)\left(L - (\delta-\delta_0)\right) & \\ 0 & \text{if } L \le \delta \end{cases} \tag{6}$$

where $L = L_f/2 - z/\cos(\phi)$ is the embedment length and L_f is the fibre length (see Fig. 1a). Here, z is the distance form the centre of the fibre to the crack surface and ϕ is the fibre orientation, as shown in Fig. 2(b). Furthermore, τ_0 is the bond strength at the onset of slip, β is the hardening parameter, d_f is the diameter of the fibre and $c = \beta L_f/(2d_f)$. At the displacement threshold

$$\delta_0 = \frac{L_f}{c}\left(\cosh\left(\frac{\omega L}{d_f}\right) - 1\right) \tag{7}$$

the debonding process is completed.

In (6),

$$\eta = \frac{V_f E_f}{V_m E_m} \tag{8}$$

and

$$\omega = \sqrt{4(1+\eta)\beta\tau_0/E_f} \tag{9}$$

where E_f and E_m are Young's moduli and V_f and $V_m = 1 - V_f$ are volume fractions of fibre and concrete matrix, respectively. For our modified model described in Section 3.2, a spatial variation of the fibre distribution is considered, which is explained in the calibration part of Section 4. In [11], it is assumed that one-sided pullout occurs. Therefore, the pullout displacement is equal to the crack opening. The pullout force versus crack opening is shown in Fig. 1a for $z = 0$ and $\phi = 0$, where the displacement (crack opening) is normalised by dividing it with $L_f/2$ and the force is normalised by dividing it with the force at δ_0. The expression in (6) was derived in [11] based on the assumption that the fibre is rigid. Therefore, for plotting Fig. 1a, the stiffness ratio E_f/E_m was set to 200 so that the force approaches zero at a displacement of $L_f/2$. As seen in Fig. 1a, the response is strongly influenced by the parameter β, which controls the hardening response at the fibre scale [11]. The greater β is, the greater is the crack opening at which the maximum bridging stress is reached. This parameter enters the expression of c, which will play an important part in the development of our model in Section 4.

The bridging stress σ_f acting on a crack surface as function of the crack opening δ was proposed in [11] as

$$\sigma_f = \frac{4V_f}{\pi d_f^2}\int_{\phi=0}^{\pi/2}\int_{z=0}^{(L_f/2)\cos\phi} P(\delta)\, g(\phi)\, p(\phi)\, p(z) \mathrm{d}z \mathrm{d}\phi \tag{10}$$

Here, $P(\delta)$ is the pullout force of one fibre across one crack. Furthermore, $p(\phi) = \sin\phi$ is the probability density function of inclination angle ϕ and $g(\phi) = \exp(f\phi)$ which includes the snubbing factor f. This factor accounts for fibres being inclined at the crack plane as shown in Fig. 2a. Furthermore, $p(z) = 2/L_f$ is the probability density function of the shortest distance from the centre of fibre to the crack plane, which is assumed to be uniformly distributed for $0 < z < L_f/2$ [11].

Integrating (10) numerically is computationally demanding, if it has to be carried out many times within finite element simulations. Lin and Li [11] derived an approximate closed-form solution of (10) as

$$\tilde{\sigma}_f = \frac{\sigma_f}{\sigma_0} = \begin{cases} \dfrac{2}{k}\left[1 - \dfrac{1}{k}\cosh^{-1}\left(1 + \lambda\dfrac{\tilde{\delta}}{\tilde{\delta}^*}\right)\right]\sqrt{\left(1+\lambda\dfrac{\tilde{\delta}}{\tilde{\delta}^*}\right)^2 - 1} + \dfrac{2\lambda\tilde{\delta}}{k^2\tilde{\delta}^*} & \text{if } 0 \le \tilde{\delta} \le \tilde{\delta}^* \\ \left(1 + c\tilde{\delta}\right)\left(1-\tilde{\delta}\right)^2 & \text{if } \tilde{\delta}^* \le \tilde{\delta} \le 1 \\ 0 & \text{if } 1 \le \tilde{\delta} \end{cases} \tag{11}$$

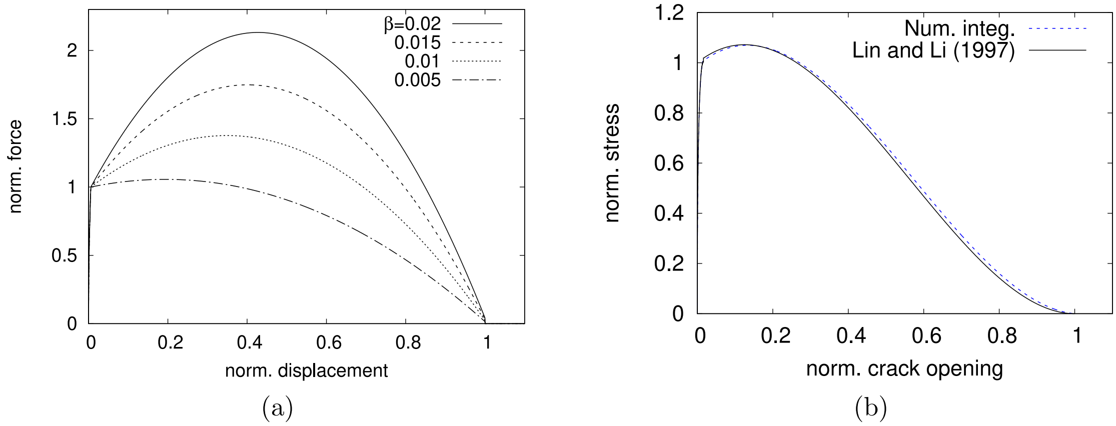

Fig. 1. Original fibre model according to [11]: (a) Normalised pullout force versus normalised crack opening. (b) Average fibre stress versus crack opening computed from (11) and numerical integration of (10).

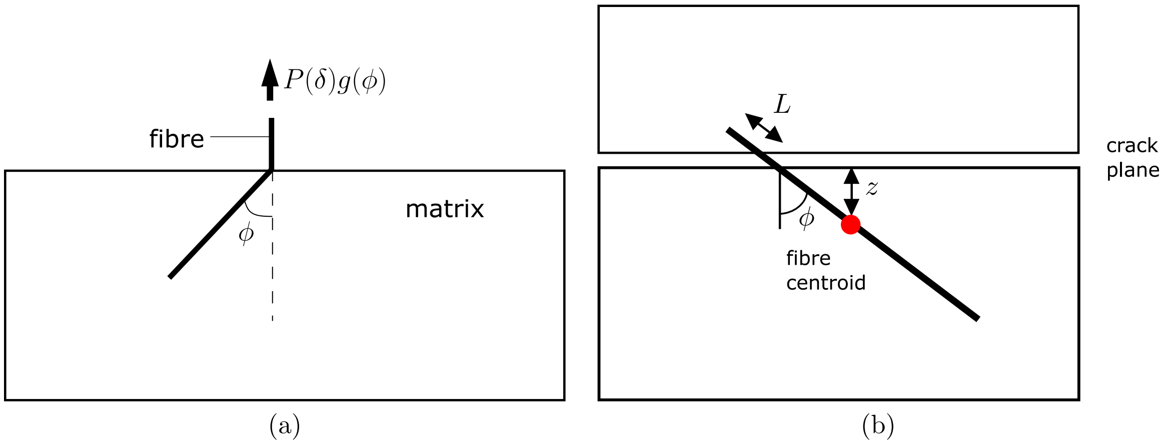

Fig. 2. Schematic illustration of (a) snubbing effect and (b) single fibre crossing a crack.

where $\tilde{\delta} = 2\delta/L_f$ is the normalised crack opening and $k = \omega L_f/\left(2d_f\right)$. Furthermore, the reference stress at the end of debonding without hardening is

$$\sigma_0 = \frac{1}{2} g \tau_0 V_f (1+\eta) L_f/d_f \tag{12}$$

The normalised crack opening at the end of the debonding stage is

$$\tilde{\delta}^* = \frac{2\lambda}{c} \tag{13}$$

where

$$\lambda = \cosh(k) - 1 \tag{14}$$

Furthermore,

$$g = \frac{2}{4+f^2}\left(1+\exp(\pi f/2)\right) \tag{15}$$

A comparison of the numerical integration of (10) and the approximate solution in (11) is shown in Fig. 1b. It can be seen that (11) is overall in good agreement with the numerical integration. However, there is a jump in the curve predicted by (11), which can produce numerical difficulties if (11) is used as part of an iterative approach within a constitutive model for finite element analysis. We address this problem in the next section.

3.2. Reformulate fibre stress-crack opening law

The approximate solution of the fibre bridging stress in (11) exhibits a jump at $\tilde{\delta} = \tilde{\delta}^*$ as shown in Fig. 3a and b, which results in numerical problems when the bridging stress in (11) is used within the damage-plasticity model in (4) to determine the damage

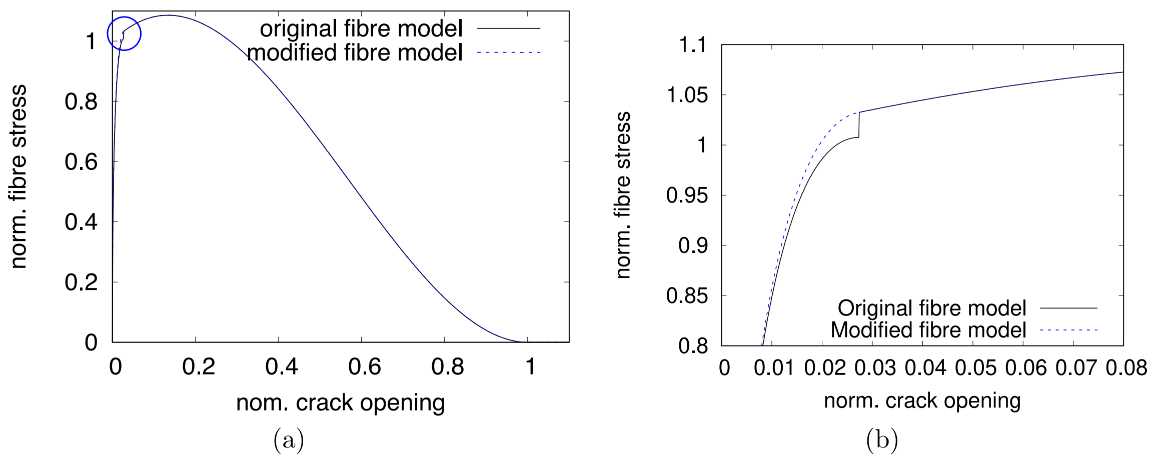

Fig. 3. Fibre stress versus crack opening for approximate relation with jump at $\tilde{\delta} = \tilde{\delta}^*$ and proposed modification without jump: (a) full curve, (b) zoom to area around $\tilde{\delta} = \tilde{\delta}^*$.

variable iteratively. The jump is present because of simplifications in the integration of (10) for the pullout part of the fibres. For $0 \leq \tilde{\delta} \leq \tilde{\delta}^*$, the bridging stress in (10) is composed of

$$\tilde{\sigma}_{\mathrm{f}} = \tilde{\sigma}_{\mathrm{f}}^{\mathrm{debonding}} + \tilde{\sigma}_{\mathrm{f}}^{\mathrm{pullout}} \tag{16}$$

Here $\tilde{\sigma}_{\mathrm{f}}^{\mathrm{debonding}}$ and $\tilde{\sigma}_{\mathrm{f}}^{\mathrm{pullout}}$ are fibre stresses due to debonding and pullout, respectively, which are present before all fibres are debonded. The pullout part is represented in (11) by the term

$$\tilde{\sigma}_{\mathrm{f}}^{\mathrm{pullout}} = 2\lambda\tilde{\delta}/(k^2\tilde{\delta}^*) \tag{17}$$

Furthermore, we know that $\tilde{\sigma}^{\mathrm{debonding}} = 0$ at $\tilde{\delta} = \tilde{\delta}^*$ since $\tilde{\delta}^*$ is the crack opening at which all fibres are fully debonded. Therefore, we propose to resolve this jump by adding a linear function to the pullout part so that the new pullout part of the bridging stress for $\tilde{\delta} \leq \tilde{\delta}^*$ as

$$\tilde{\sigma}_{\mathrm{f}}^{\mathrm{pullout}} = 2\lambda\tilde{\delta}/(k^2\tilde{\delta}^*) + a\tilde{\delta}/\tilde{\delta}^* \tag{18}$$

Here, the parameter a is determined by enforcing zero jump of the bridging stress expressions for $\tilde{\delta} \leq \tilde{\delta}^*$ and $\tilde{\delta} \geq \tilde{\delta}^*$ at $\tilde{\delta} = \tilde{\delta}^*$, which results in

$$2\lambda/k^2 + a = \left(1 + c\tilde{\delta}^*\right)\left(1 - \tilde{\delta}^*\right)^2 \tag{19}$$

Solving (19) for a gives

$$a = \left(1 + c\tilde{\delta}^*\right)\left(1 - \tilde{\delta}^*\right)^2 - 2\lambda/k^2 \tag{20}$$

so that the new expression for the pullout part of the bridging stress is

$$\tilde{\sigma}^{\mathrm{pullout}} = 2\lambda\tilde{\delta}/(k^2\tilde{\delta}^*) + \left[\left(1 + c\tilde{\delta}^*\right)\left(1 - \tilde{\delta}^*\right)^2 - 2\lambda/k^2\right]\tilde{\delta}/\tilde{\delta}^* \tag{21}$$

This is a function of fibre and matrix parameters only. Consequently, the bridging stress formulation that we use for this work is

$$\tilde{\sigma}_f = \frac{\sigma_f}{\sigma_0} = \begin{cases} \frac{2}{k}\left[1 - \frac{1}{k}\cosh^{-1}\left(1 + \lambda\frac{\tilde{\delta}}{\tilde{\delta}^*}\right)\right]\sqrt{\left(1 + \lambda\frac{\tilde{\delta}}{\tilde{\delta}^*}\right)^2 - 1} + & \\ \frac{2\lambda\tilde{\delta}}{k^2\tilde{\delta}^*} + \left[\left(1 + c\tilde{\delta}^*\right)\left(1 - \tilde{\delta}^*\right)^2 - 2\lambda/k^2\right]\tilde{\delta}/\tilde{\delta}^* & \text{if } 0 \leq \tilde{\delta} \leq \tilde{\delta}^* \\ \left(1 + c\tilde{\delta}\right)\left(1 - \tilde{\delta}\right)^2 & \text{if } \tilde{\delta}^* \leq \tilde{\delta} \leq 1 \\ 0 & \text{if } 1 \leq \tilde{\delta} \end{cases} \tag{22}$$

which provides a reasonable agreement with the solution obtained from numerical integration.

4. Link between cracking strain and crack opening

The aim of the present work is to incorporate a micro-mechanics based fibre model into a macroscopic constitutive model, which is based on stress–strain relations and in which the inelastic processes are represented by a cracking strain as a function of a damage variable. Therefore, we require a link of the crack opening δ to the cracking strain $\varepsilon_{\mathrm{cr}}$ used in (4).

As mentioned before, SHCC materials subjected to tension exhibit distributed cracking, because of the slip hardening pullout response of individual fibres. For displacements greater than the displacement at which the bridging stress reaches its maximum, softening occurs which is accompanied by the formation of a single localised crack. For converting crack opening to cracking strain, we are required to know the crack opening at which the softening process starts. With this information, we use then the crack band approach for the localised part of the cracking response, i.e. we scale the cracking strain with respect to the element length to obtain mesh independent results [23]. We assume that the matrix is so brittle in comparison to the fibre response, that the condition for softening is given by the fibre response only.

Independently of c, the debonding phase exhibits always hardening so that the earliest that softening can occur is when $\tilde{\delta} = \tilde{\delta}^*$. Therefore, we can focus our attention on the part of the fibre stress function in which $\tilde{\delta} \geq \tilde{\delta}^*$. For softening to occur, the condition $\mathrm{d}\tilde{\sigma}_f/\mathrm{d}\tilde{\delta} = 0$ has to be met. Differentiating $\tilde{\sigma}_\mathrm{f}$ in (22) with respect to $\tilde{\delta}$ for $\tilde{\delta} \geq \tilde{\delta}^*$ and setting it to zero results in

$$\frac{\mathrm{d}\tilde{\sigma}_f}{\mathrm{d}\tilde{\delta}} = \left(\tilde{\delta} - 1\right)\left(3c\tilde{\delta} - c + 2\right) = 0 \tag{23}$$

Let us first study the case that softening occurs at the end of debonding. Setting $\tilde{\delta} = \tilde{\delta}^*$ into (23) and using the expression for $\tilde{\delta}^*$ in (13), we obtain a condition for the onset of softening at $\tilde{\delta} = \tilde{\delta}^*$, which is $c = 6\lambda + 2$. Therefore, for $c \leq 6\lambda + 2$ softening occurs at the end of debonding, i.e. $\tilde{\delta}_\mathrm{cu} = \tilde{\delta}^* = 2\lambda/c$. On the other hand, for $c > 6\lambda + 2$, softening will occur when the condition $\mathrm{d}\tilde{\sigma}_f/\mathrm{d}\tilde{\delta} = 0$ is met for $\tilde{\delta} > \tilde{\delta}^*$. The present study is limited to fibre arrangements which exhibit strain hardening beyond $\tilde{\delta} > \tilde{\delta}^*$, i.e. $c > 6\lambda + 2$. For this case, the displacement at the onset of softening $\tilde{\delta} = \tilde{\delta}_\mathrm{cu}$ is obtained by solving (23), which gives $\tilde{\delta}_\mathrm{cu} = (c-2)/(3c)$. The other solution to (23) is that $\tilde{\delta} = 1$, which is the case of complete pullout and is not of interest here.

Therefore, the critical displacement at which softening occurs is

$$\tilde{\delta}_\mathrm{cu} = \begin{cases} 2\lambda/c & \text{if } c \leq 6\lambda + 2 \\ (c-2)/(3c) & \text{if } c > 6\lambda + 2 \end{cases} \tag{24}$$

The corresponding critical stress $\tilde{\sigma}_\mathrm{cu}$ is obtained by setting (24) into (22) which results after mathematical manipulations in

$$\tilde{\sigma}_\mathrm{cu} = \begin{cases} (1+2\lambda)(2\lambda/c - 1)^2 & \text{if } c \leq 6\lambda + 2 \\ \dfrac{4(c+1)^3}{27c^2} & \text{if } c > 6\lambda + 2 \end{cases} \tag{25}$$

The information about $\tilde{\delta}_\mathrm{cu}$ and $\tilde{\sigma}_\mathrm{cu}$ can now be used to develop a link between the cracking strain ε_cr and the crack opening δ.

In the present study, we propose for hardening to link the crack opening to the cracking strain for $\varepsilon_\mathrm{cr} < \varepsilon_\mathrm{cu}$ as

$$\delta(\varepsilon_\mathrm{cr}) = \delta_\mathrm{cu} \frac{1 - \exp\left(-\dfrac{\epsilon_\mathrm{cr}}{\xi}\right)}{1 - \exp\left(-\dfrac{\epsilon_\mathrm{cu}}{\xi}\right)} \tag{26}$$

where $\varepsilon_\mathrm{cu} = \gamma_\mathrm{cu}\delta_\mathrm{cu}/s_\mathrm{m}$ is the cracking strain at the peak of the bridging stress and s_m is the saturated crack spacing. Here, ξ is a parameter, which controls the slope of the relationship between the maximum displacement and the cracking strain at maximum bridging stress. Furthermore, γ_cu is a parameter, which originates from the variation of fibres and relates the average crack opening $\bar{\delta}_\mathrm{cu}$ to the maximum crack opening δ_cu at maximum bridging stress as $\bar{\delta}_\mathrm{cu} = \gamma_\mathrm{cu}\delta_\mathrm{cu}$. For $\varepsilon_\mathrm{cr} = \varepsilon_\mathrm{cu}$, (26) results in $\delta(\varepsilon_\mathrm{cr}) = \delta_\mathrm{cu}$. The link between γ_cu and the variation of fibres is explained in Section 5.

Once softening is initiated, i.e. $\delta(\varepsilon_\mathrm{cr}) = \delta_\mathrm{cu}$, only one crack continues to open while the other cracks are unloading. For softening, we use the crack band approach to obtain mesh-independent results [23]. For this part of the model, the crack opening as a function of the cracking strain is modelled by a transition from the saturated crack spacing s_m at the peak of the bridging stress-crack opening curve to the element length h_e at the point at which the bridging stress is equal to zero. We assume that the unloading of cracks occurs to the origin without any irreversible crack opening. This is in acceptable agreement with the macroscopic constitutive model in which the current bridging stress relation is embedded (see Section 2), which exhibits in tension negligible irreversible inelastic strains. In our simulations in Section 6, the hardening modulus H_p is chosen large enough to reproduce the hardening response prescribed by (22) correctly. With this hardening modulus, the plastic strain in tension is small. However, in compression there is still significant plastic strain, which is important for modelling shear, because plasticity provides volumetric–deviatoric coupling which isotropic damage does not provide [24].

First, we consider $s_\mathrm{m}/\gamma_\mathrm{cu} < h_\mathrm{e}$, i.e. there are more than one crack in a finite element. For $\gamma_\mathrm{cu} < 1$, the crack openings vary within one element. During hardening, the crack opening of all cracks increases. At the onset of softening, the crack with the largest opening has reached δ_cu. The other cracks have smaller crack openings at the same stress, because the volume fraction of these cracks is greater than for the one crack in which δ_cu is reached first. The average of these smaller crack openings at the onset of softening is called here $\delta_\mathrm{cu}^\mathrm{un}$. As softening progresses, the crack with the greatest opening continues to open while the other cracks will close. The schematics of two different crack openings is shown in Fig. 4 Based on this assumption, we write for the onset of softening

$$\varepsilon_\mathrm{cu} h_\mathrm{e} = \gamma_\mathrm{cu}\frac{\delta_\mathrm{cu}}{s_\mathrm{m}} h_\mathrm{e} = \delta_\mathrm{cu} + \delta_\mathrm{cu}^\mathrm{un}\left(\frac{h_\mathrm{e}}{s_\mathrm{m}} - 1\right) \tag{27}$$

Here, δ_cu and $\delta_\mathrm{cu}^\mathrm{un}$ are the crack openings of the localised and unloading cracks, respectively, at the onset of softening.

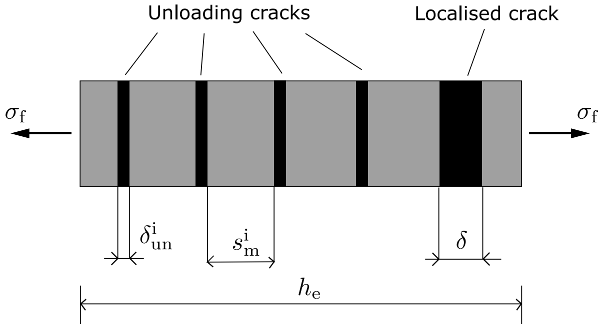

Fig. 4. Schematics of δ_{cu} and δ^{un}_{cu} onset of softening when $s_m/\gamma_{cu} < h_e$.

Consequently, the unloading displacement at the onset of softening is expressed in form of the maximum crack opening as

$$\delta^{un}_{cu} = \delta_{cu}\frac{\gamma_{cu}h_e - s_m}{h_e - s_m} \tag{28}$$

For the derivation of the link between cracking strain and crack opening during softening, we distinguish again between two crack openings. The first one is the average crack opening δ^{un} of the unloading cracks and the second one is the crack opening δ of the widening crack in which the displacements are localised. The bridging stress of the two types of cracks must be the same to satisfy equilibrium. Therefore, the unloading displacement is determined as

$$\delta^{un} = \frac{\delta^{un}_{cu}}{\sigma_{cu}}\sigma_f = \frac{\delta^{un}_{cu}}{\sigma_{cu}}\sigma_0\left(1+\frac{\beta\delta}{d_f}\right)\left(1-2\delta/L_f\right)^2 \tag{29}$$

where σ_f is the bridging stress determined from the crack opening δ of the crack in which the displacements localise according to (22). The cracking strain is then the sum of the crack openings divided by the element length h_e, which results in

$$\varepsilon_{cr} = \left(\delta + \left(h_e/s_m - 1\right)\delta_{un}\right)/h_e \tag{30}$$

Setting δ^{un} in (29) into (30) results in

$$\varepsilon_{cr} = \frac{1}{h_e}\left(\delta + \left(h_e/s_m - 1\right)\frac{\delta^{un}_{cu}}{\sigma_{cu}}\sigma_0\left(1+\frac{\beta\delta}{d_f}\right)\left(1-2\delta/L_f\right)^2\right) \tag{31}$$

From this function, δ is determined iteratively. To avoid local snapback, i.e. snapback at the constitutive level, ε_{cr} must increase with increasing δ, which provides an upper limit for the element size h_e. This upper limit is determined by setting the second derivative of (31) with respect to δ equal to zero and solve for the critical displacement at which the slope of the softening curve is the steepest. This displacement is then set into the first derivative of (31) with respect to δ, which has to be greater than zero. This provides then an inequality for h_e, which needs to be satisfied to avoid local snapback. The first derivative of (31) with respect to δ is

$$\frac{d\varepsilon_{cr}}{d\delta} = \frac{1}{h_e}\left\{1 + \frac{9c\,(c-2)\left(2\delta/L_f - 1\right)\left(\gamma_{cu}h_e/s_m - 1\right)\left[c\left(2\delta/L_f - 1\right) + 2\left(2c\delta/L_f + 1\right)\right]}{4\,(c+1)^3}\right\} \tag{32}$$

and the second derivative is

$$\frac{d^2\varepsilon_{cr}}{d\delta^2} = \frac{9c\left(\gamma_{cu}h_e - s_m\right)(c-2)\left(L_f - 2L_f c + 6c\delta\right)}{L_f^2 h_e s_m\,(c+1)^3} \tag{33}$$

These derivatives are rather complicated, but the critical displacement at the steepest softening and the limit on the element length are of compact form. By setting (33) equal to zero and solving for δ, the critical displacement at which the softening is the steepest is determined as $\delta = \delta_{crit} = L_f(2c-1)/(6c)$. Inserting $\delta = \delta_{crit}$ into (32), setting (32) equal to zero and solving it for the element length h_e gives

$$h_e = h_e^{crit} = (7c-2)s_m/(\gamma_{cu}(3c-6)) \tag{34}$$

Since this derivation is for $h_e > s_m/\gamma_{cu}$, the expression in (31) is valid for elements in the range $s_m/\gamma_{cu} < h_e < (7c-2)s_m/(\gamma_{cu}(3c-6))$.

Let us now consider the case that $h_e < s_m/\gamma_{cu}$. This case arises if a fine mesh is used in the numerical analysis. This means that there is no displacement in the element which will unload and the displacement at peak in the element is less than the crack opening. A reduction factor γ_0, which links the crack opening to the displacement at peak, is determined as

$$\gamma_{r0} = \frac{\gamma_{cu}}{s_m}h_e \tag{35}$$

Thus, the reduction factor results in $\gamma_{r0} = \gamma h_e/s_m$ at peak. Since for the crack band model, the displacements are localised in one row/band of elements, the reduction factor needs to increase so that at the end $\gamma_r = 1$ and the cracking strain is defined at zero fibre stress as $\varepsilon_{cr} = L_f/2/h_e$. We choose here a linear transition of the reduction factor so that $\gamma_r = \gamma_{r0} + (1-\gamma_{r0})(\delta - \delta_{cu})/(L_f/2 - \delta_{cu})$. The cracking strain results in

$$\varepsilon_{cr} = \frac{\gamma_r \delta}{h_e} = \frac{\gamma_{r0}\delta}{h_e} + \frac{(1-\gamma_{r0})(\delta^2 - \delta_{cu}\delta)}{h_e\left(L_f/2 - \delta_{cu}\right)} \tag{36}$$

For $\delta = \delta_{cu}$, we obtain $\varepsilon_{cr} = \gamma_{r0}\delta_{cu}/h_e$. For $\delta = L_f/2$, we have $\varepsilon_{cr} = L_f/(2h_e)$. From this equation, the crack opening is determined as

$$\delta = \frac{L_f\gamma_{r0} - 2\delta_{cu} - \sqrt{L_f^2\gamma_{r0}^2 - 4\delta_{cu}\left(L_f\gamma_{r0} - \delta_{cu}\right) + 8(1-\gamma_{r0})\varepsilon_{cr}h_e\left(L_f - 2\delta_{cu}\right)}}{4(\gamma_{r0} - 1)} \tag{37}$$

With this δ, the fibre stress can be calculated using (22). With the softening law derived, all parts of the bridging stress cracking strain law are complete. The fibre stress is now defined as a function of the cracking strain by using (26) and (31).

To summarise, we developed a link of the crack opening δ to the cracking strain ε_{cr} for the fibre part which is split into a hardening and softening part. For hardening, we have (26). For softening, we need to consider multiple cases. For $s_m/\gamma_{cu} < h_e$, we determine the crack opening iteratively from (31). For $s_m/\gamma_{cu} > h_e$, the explicit expression in (37) is used. The softening part of the model provided by (31) and (37) is only valid for $h_e < (7c-2)s_m/(\gamma_{cu}(3c-6))$. Furthermore, the entire derivation is for strain hardening fibre arrangements with $c > 2 + 6\lambda$.

5. Calibration

The calibration of CDPM2F, which is an extension of CDPM2 to strain hardening materials is split into two parts. First, the calibration of CDPM2 is addressed. Then, the calibration of the fibre model is discussed.

The input parameters for the matrix are those of the CDPM2 model. Many of the input parameters of CDPM2 have default values, which are used in this study and are described in [20]. We assume in this study that these parameters apply also to the matrix of SHCC. Five parameters of CDPM2 do not have default values and are required to be determined. These parameters are the Young's modulus E_m, the tensile strength f_t, the compressive strength f_c and the crack opening threshold in tension δ_f, which for the present exponential law in (5) is calculated from the fracture energy G_F as $\delta_f = G_F/f_t$. Furthermore, Poisson's ratio ν of the matrix is required. In addition to these five parameters, there is the strain threshold ε_f which controls the softening response in compression. Furthermore, the hardening modulus was set for all analyses to $H_p = 0.05$ to ensure that for the majority of the stress–strain response the effective stress is greater than the fibre stress.

For the fibre model, nine input parameters are required for the fibre stress–strain relation. Some of these parameters can be directly obtained from the specifications of the fibre manufactures and the design of the material. These parameters are Young's modulus of fibres E_f, length of fibre L_f, diameter of fibre d_f. The next group of input parameters are related to the fibre stress versus crack opening law. These parameters are the volume fraction V_f, shear strength of interface τ_0, hardening parameter β, the snubbing factor f. Furthermore, there are the parameters ξ and γ_{cu}, which control the relation of crack opening and cracking strain. Here, V_f and γ_{cu} are two parameters which depend on the spatial variation of the distribution of fibres and are calculated indirectly using the uniform volume fraction V_{f0} and the fibre distribution coefficient α, which represents the degree of variation of the spatial fibre distribution [25].

We assume that we can link the fibre volume fraction V_f at a cracked section to the dispersion as

$$\alpha = \exp\frac{V_f - V_{f0}}{V_{f0}} \tag{38}$$

so that

$$V_f = (1 + \ln\alpha)V_{f0} \tag{39}$$

There is a lower limit for α so that strain hardening is guaranteed. The condition for strain hardening is

$$\sigma_{cu} = \sigma_0\bar{\sigma}_{cu} \geq f_t \tag{40}$$

Using the expression for $\bar{\sigma}_{cu}$ in (25) and σ_0 in (12) we obtain

$$\frac{1}{2}g\tau_0V_f(1+\eta)\frac{L_f}{d_f}\frac{4(c+1)^3}{27c^2} \geq f_t \tag{41}$$

For the minimum volume $V_f = V_{f,min}$, which is required to provide a bridging stress equal to f_t, we write

$$\frac{1}{2}g\tau_0V_{f,min}(1+\eta)\frac{L_f}{d_f}\frac{4(c+1)^3}{27c^2} = f_t \tag{42}$$

Here, η is a function of $V_{f,min}$ according to (8). Also, the factor L_f/d_f is linked to c. Using these two expressions, we obtain

$$\left(E_f - E_m\right)V_{f,min}^2 + \left(E_m + E_mZ\right)V_{f,min} - E_mZ = 0 \tag{43}$$

where

$$Z = \frac{27f_t\beta}{4\,g\tau_0}\frac{c}{(c+1)^3} \tag{44}$$

Now, from (43), we obtain

$$V_{\mathrm{f,min}} = \frac{-\left(E_{\mathrm{m}} + E_{\mathrm{m}} Z\right) + \sqrt{\left(E_{\mathrm{m}} + E_{\mathrm{m}} Z\right)^2 + 4\left(E_{\mathrm{f}} - E_{\mathrm{m}}\right) E_{\mathrm{m}} Z}}{2\left(E_{\mathrm{f}} - E_{\mathrm{m}}\right)} \tag{45}$$

We set now $V_{\mathrm{f,min}}$ into the expression for α in (38) which gives

$$\alpha_{\min} = \exp \frac{V_{\mathrm{f,min}} - V_{\mathrm{f0}}}{V_{\mathrm{f0}}} \tag{46}$$

Here, $\alpha_{\min}$ is the lower limit of α, so that the region with a critically low fibre distribution still exhibits strain hardening.

Parameter γ_{cu} depends also on α. We assume that γ_{cu} is a linear function of α as

$$\gamma_{\mathrm{cu}} = \frac{(1-\alpha)\,\varepsilon_0 s_{\mathrm{m}}}{\delta_{\mathrm{cu}}\left(1-\alpha_{\min}\right)} + \frac{\alpha - \alpha_{\min}}{1-\alpha_{\min}} \tag{47}$$

which is motivated by experimental results in [25,26]. Let us explore (47). For $\alpha = \alpha_{\min}$, we have $\gamma_{\mathrm{cu}} = \varepsilon_0 s_{\mathrm{m}}/\delta_{\mathrm{cu}}$. Thus, $\varepsilon_{\mathrm{cu}} = \gamma_{\mathrm{cu}}\delta_{\mathrm{cu}}/s_{\mathrm{m}} = \varepsilon_0$. For the other limit, let us consider the case of a fibre reinforced specimen at ultimate stress σ_{cu} for which all cracks exhibit the same crack opening and are equally spaced, which corresponds to $\alpha = 1$, i.e. fibres are uniformly distributed within the volume. For this idealised assumption, $\gamma_{\mathrm{cu}} = 1$ and, therefore, $\varepsilon_{\mathrm{cu}} = \delta_{\mathrm{cu}}/s_{\mathrm{m}}$. This concludes the calibration of the model.

CDPM2F is implemented in the open source finite element program OOFEM [27]. The implementation of the procedure for the computation of the effective stress and the compressive damage variable is the same as in CDPM2. For determining the tensile damage variable, three steps are carried out. First, the cracking strain is converted into crack opening. Then, the fibre and matrix stresses are computed as function of the crack opening. Finally, the damage variable is determined iteratively from the balance of nominal stress and sum of fibre and concrete stress.

6. Material response

The stress–strain law derived in the previous sections is aimed to evaluate the tensile response of SHCC based on micro mechanical properties of fibres and matrix. By incorporating this law into CDPM2 to form CDPM2F, a tool is available to predict the structural response of SHCC members in 3D. In this section, CDPM2F is applied to simulate the performance of structural members subjected to tension, shear and compression. The model response is compared to experiments in which the matrix is made of engineered cementitious composites (ECC), which is one type of SHCC.

6.1. Tension

The first example is a tensile test of an ECC specimen reported in [28]. The geometry with loading setup and the medium finite element mesh with an element size of 2 cm are shown in Fig. 5a and b, respectively. The out-of-plane thickness is 12.7 mm. The three-dimensional finite element mesh consists of tetrahedral elements and was generated with the mesh generator T3D [29].

From the experiments in [28], two sets were modelled which differ mainly in fibre properties. For set 1 with short and thin fibres, the model input parameters for the matrix are Young's modulus $E_{\mathrm{m}} = 15.9$ GPa, Poisson's ratio $\nu = 0.2$, tensile strength $f_{\mathrm{t}} = 1.12$ MPa, compressive strength $f_{\mathrm{c}} = 15.5$ MPa and crack opening threshold $\delta_{\mathrm{f}} = 0.01$ mm. Here, E_{m} and f_{c} were chosen from [28]. Tensile strength f_{t} was chosen to be smaller than in the experiments to avoid initial softening in the constitutive response. The stress is composed of fibre stress and matrix stress. The matrix stress reaches its maximum at a much smaller strain than the fibre stress. Therefore, it could be that after the matrix stress reaches its maximum the decrease of the matrix stress (softening) is greater than the increase of the fibre stress (hardening). This would then lead to a decrease of the overall stress even if the final fibre bridging stress is greater than the sum of fibre and matrix stress when the matrix stress reaches its maximum. The parameters ν and δ_{f} were given typical values for mortar. The fibre properties are Young's modulus $E_{\mathrm{f}} = 60$ GPa, length $L_{\mathrm{f}} = 6$ mm, fibre diameter $d_{\mathrm{f}} = 0.014$ mm, $f = 0.5$, $\beta = 0.015$, $\tau_0 = 1.8$ MPa, $s_{\mathrm{m}} = 12$ mm, $\xi = 10$, $\alpha = 0.53$ and $V_{\mathrm{f0}} = 0.015$. The last two parameters result in $\gamma_{\mathrm{cu}} = 0.2$ and $V_{\mathrm{f}} = 0.0055$. These fibre properties result in $c = \beta L_{\mathrm{f}}/\left(2d_{\mathrm{f}}\right) = 3.2$. Here, E_{f}, L_{f}, d_{f} and V_{f0} are chosen from [28]. The other parameters were given reasonable values for ECC so that the response agreed with the experimental results.

For set 2 with long and thick fibres, the model input parameters for the matrix are Young's modulus $E_{\mathrm{m}} = 15.9$ GPa, Poisson's ratio $\nu = 0.2$, tensile strength $f_{\mathrm{t}} = 1.12$ MPa, compressive strength $f_{\mathrm{c}} = 15.5$ MPa and crack opening threshold $\delta_{\mathrm{f}} = 0.01$ mm. Again, E_{m} and f_{c} were chosen from [28]. Tensile strength f_{t} was chosen to be smaller than in the experiments to avoid initial softening in the constitutive response The parameters ν and δ_{f} were given typical values for mortar. The fibre properties are Young's modulus $E_{\mathrm{f}} = 60$ GPa, length $L_{\mathrm{f}} = 12$ mm, fibre diameter $d_{\mathrm{f}} = 0.04$ mm, $f = 0.5$, $\beta = 0.015$, $\tau_0 = 1$ MPa, $s_{\mathrm{m}} = 4$ mm, $\xi = 10$, $\alpha = 0.59$ and $V_{\mathrm{f0}} = 0.02$. The last two parameters result in $\gamma_{\mathrm{cu}} = 0.23$ and $V_{\mathrm{f}} = 0.00094$. This gives $c = \beta L_{\mathrm{f}}/\left(2d_{\mathrm{f}}\right) = 2.3$. Again, E_{f}, L_{f}, d_{f} and V_{f0} are chosen from [28]. The other parameters were given reasonable values for ECC so that the response agreed with the experimental results. The end areas of the specimen shown in dark grey in Fig. 5 are modelled as aluminium with Young's modulus of 70 GPa and Poisson's ratio of $\nu = 0.2$. The comparison of FE model and experiments is shown in Fig. 6 in the form of stress versus strain for the mesh with an element size of 2 cm. Here, stress is the force divided by the cross-sectional area and strain is the end displacement of the specimen divided by the length.

CDPM2F produces for the tensile response of ECC with the two fibre properties results which are in good agreement with the experiments. As expected from the expression of $\tilde{\sigma}_{\mathrm{cu}}$ in (25), the set with greater c produces the greater bridging stress.

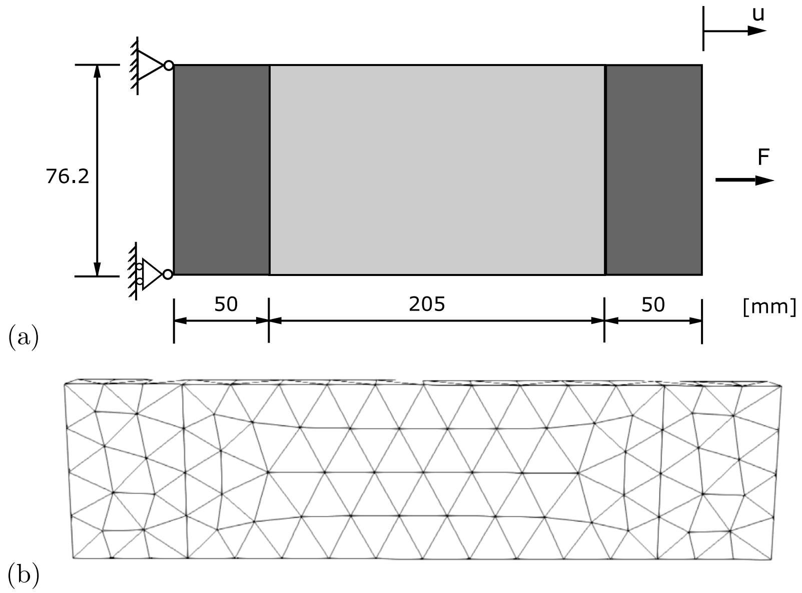

Fig. 5. (a) Tensile test setup used in the model based on the experiments reported in [28]; (b) Medium three-dimensional tetrahedral finite element mesh with element size 2 cm. The out-of-plane thickness is 12.7 mm.

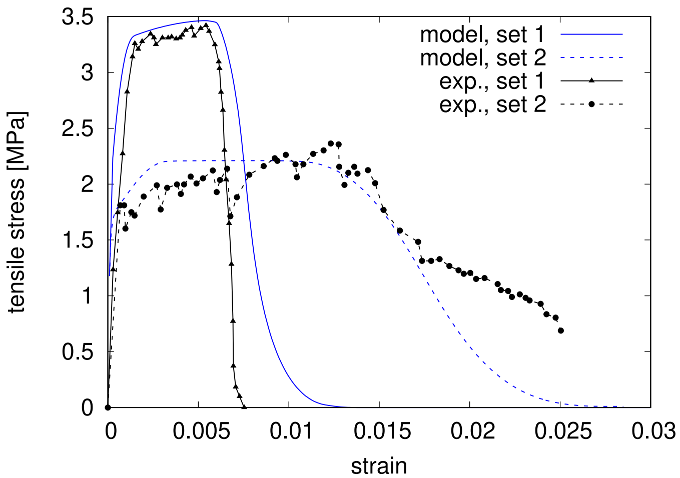

Fig. 6. Comparison of set 1 and 2 of finite element model with element size 0.02 m with experimental results reported in [28].

Next, it is checked that the model does not exhibit pathological mesh-dependence. Coarse, medium and fine meshes with element sizes of 4, 2 and 1 cm, respectively, are used for the ECC with short fibres. The input is the same as for the comparison with the experiments. The results are shown in the form of tensile stress versus strain in Fig. 7. The first part of the response up to the onset of softening is mesh independent. For the softening part a difference in the curves is present. However, for all three curves softening starts at the same strain and also reach zero stress at the same strain. The pre- and post-peak responses can be further understood by studying the strain profiles for the three meshes. For the hardening part, the strain contours are shown in Fig. 8 at an average strain of 0.004 in Fig. 7.

The strains are more or less uniform in the concrete specimen and independent of the mesh size. Slightly higher strains are visible close to the ends of the ECC specimen next to the aluminium plates due to the higher stiffness of the plates which constraints the ECC material in the lateral direction. The ECC material is strain hardening at this stage of the analysis.

In Fig. 9, the maximum principal strain contours are shown at an average strain of 0.012 in Fig. 7. At this softening stage of the analyses, strain is localised in mesh dependent zones as assumed for the crack band approach. The difference between the curves for the meshes in the softening regime is explained by the link between crack opening and cracking strain defined in (37). With the input chosen for the present comparison to the experiments in [28], we have $h_e < s_m/\gamma_{cu}$. Therefore, the reduction factor determined in (35) is used in the simulations, which varies linearly during softening.

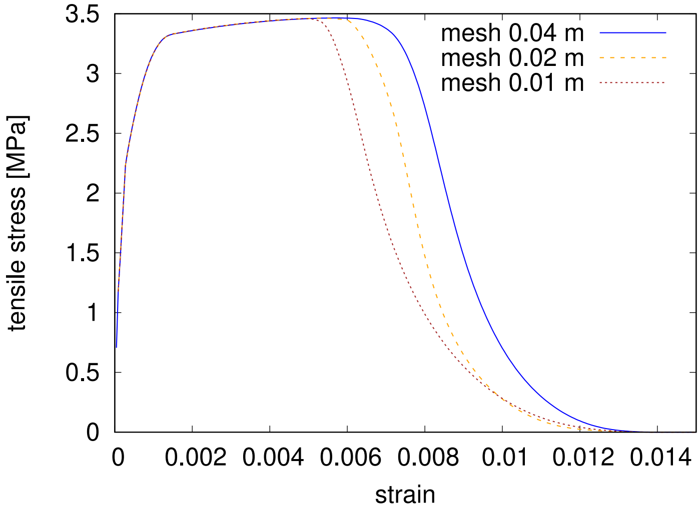

Fig. 7. Convergence of set 2 model.

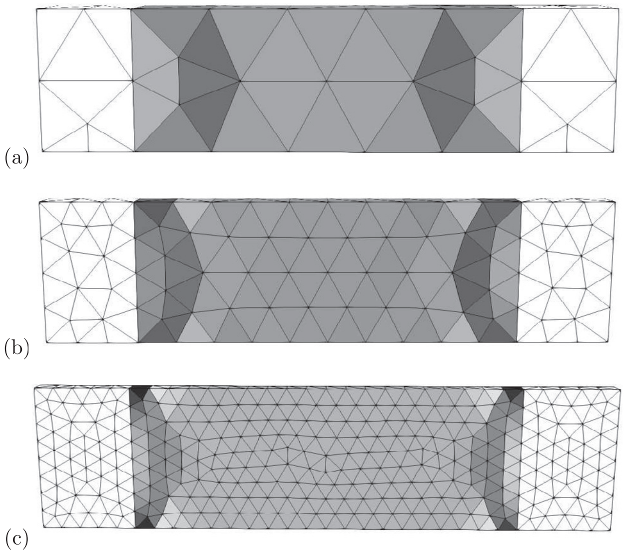

Fig. 8. Contour plot of the maximum component of the principle strain at an average strain of 0.004 for mesh sizes (a) 4 cm, (b) 2 cm and (c) 1 cm. The upper threshold for the maximum strain was chosen as 0.006.

In the tensile analyses, the hardening modulus was set to $H_p = 0.05$. This value was chosen because it allows for a good representation of the debonding stage of the tensile test as shown in Fig. 10. Larger values of H_p result in less plasticity, which can be problematic in analyses in which compression plays a role.

6.2. Shear

The second example is an ECC panel subjected to shear as reported in [30]. The geometry and loading setup is shown in Fig. 11a. The specimen consists of two regions modelled to be elastic (shown as dark grey) and a middle region modelled as ECC material. The out-of-plane thickness of the specimen is 50 mm. A coarse, medium and fine mesh with element sizes of $h_e = 4$, 2 and 1 cm were used. The three-dimensional tetrahedral meshes were generated with T3D [29]. The mesh with an element size $h_e = 2$ cm is shown in Fig. 11b.

Many of the material parameters were chosen using the information provided in [30]. Some of the model parameters were calibrated to obtain a good agreement with the experimental results. For the ECC specimen, model input parameters for the matrix are Young's modulus $E_m = 20$ GPa, Poisson's ratio $\nu = 0.2$, tensile strength $f_t = 1.4$ MPa, compressive strength $f_c = 53$ MPa and

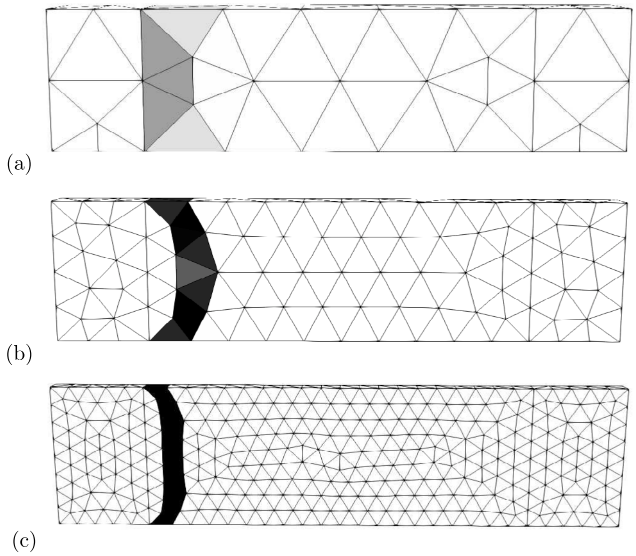

Fig. 9. Contour plot of the maximum component of the principle strain at an average strain of 0.012 for mesh sizes (a) 4 cm, (b) 2 cm and (c) 1 cm. The upper threshold for the maximum strain was chosen as 0.15.

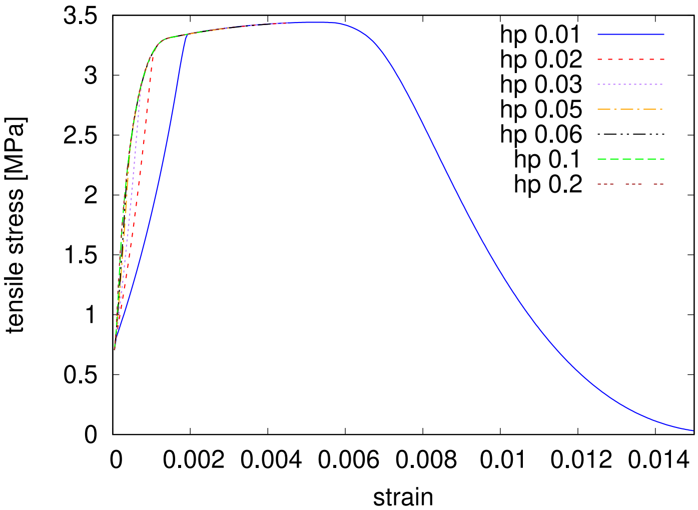

Fig. 10. Stress–strain response for set 1 with H_p values ranging from 0.01 to 0.2.

crack opening threshold $\delta_f = 0.015$ mm. Furthermore, $\varepsilon_f = 0.000085$, which is close to the default value of 0.0001. Here, E_m and f_c were chosen from [30]. The tensile strength was reduced (experimental value is 2.2 MPa) to avoid initial softening in the initial part of the stress–strain curve. The parameters ν and δ_f were given typical values for mortar. The fibre properties are Young's modulus $E_f = 48$ GPa, length $L_f = 12.7$ mm, fibre diameter $d_f = 0.04$ mm, $f = 0.8$, $\beta = 0.03$, $\tau_0 = 0.63$ MPa, $s_m = 18$ mm, $\xi = 10.$, $\alpha = 0.9$ and $V_{f0} = 0.02$. The last two parameters result in $\gamma_{cu} = 0.808$ and $V_f = 0.0179$. The parameters result in $c = \beta L_f / \left(2d_f\right) = 5.01$. Here, E_f, L_f, d_f and V_{f0} are chosen from [30]. The other parameters were given reasonable values for ECC so that the constitutive response agreed with the experimental results of ECC in tension, which are part of the same experimental study [30]. For the elastic regions, the Young's modulus is $E_m = 90$ GPa and Poisson's ratio is $\nu = 0.2$. This higher Young's modulus is chosen to represent the larger out of plane thickness in the outer region. For the flexural reinforcement, Young's modulus $E_s = 210$ MPa and a yield strength $f_{rt} = 448$ MPa were chosen. The diameter of reinforcement bar is 20 mm. The embedment length of the reinforcement in the ECC material is 60 mm. With these input parameters, the tensile stress–strain response is in reasonable agreement with the experimental results in [30] as shown in Fig. 12.

The main purpose of the shear test is to generate a constant shear force between loading points, so that the specimen is mainly subjected to shear. In the experiments in [30], the average shear strain is calculated by the measured displacements at two sets of four points in specimen as shown in Fig. 11. With these two sets A and B, the horizontal strain ε_1, vertical strain ε_2 and diagonal

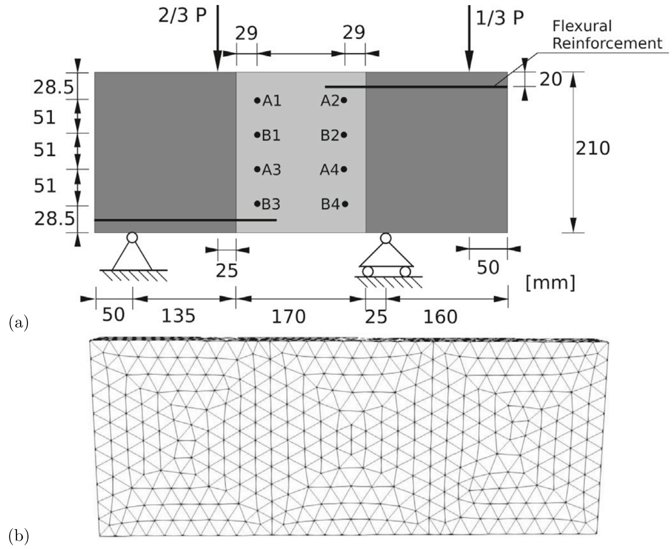

Fig. 11. (a) Geometry and setup of ECC panel subjected to shear based on [30] and (b) three-dimensional tetrahedral finite element mesh with element size of 2 cm.

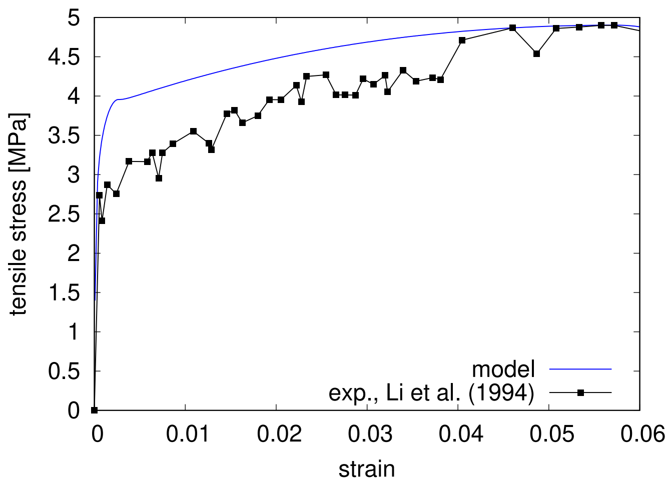

Fig. 12. Model strain–stress curve under tension compared with experimental results reported in [30].

strain ε_3 are calculated as described in [30]. From these three strain components, the engineering shear strain is calculated as

$$\gamma_{\mathrm{average}} = 2\varepsilon_3 - \varepsilon_1 - \varepsilon_2 \tag{48}$$

Here, the same approach is used for post-processing the FE results.

The comparison of shear stress and shear strain relation between model and experiment is shown in Fig. 13. The model can generally predict the trend of the shear stress and shear strain curve in the experiments. The shear strain at peak shear stress is almost same as in the experiment. However, the predicted peak shear stress is different, which might be due to the underlying CDPM2 model response and not due to the fibre extension. The first component of principle strain for the three mesh sizes at a shear strain of 0.025 is shown in Fig. 14. The strain is not localised at peak stress in the FE model. In Fig. 14, the dark areas of the contour plot represents distributed cracks because even at high values of principal strain the material is still in the hardening stage. For the small element size of $h_{\mathrm{e}} = 1$ cm, a nonuniform strain distribution can be seen, which implies that distributed cracks form more likely at the top and bottom parts of the specimen at the peak value of shear stress. To illustrate the failure process, the evolution of the principal strain for the fine mesh is shown in Fig. 15. The value of the first principle strain at the middle part of the specimen increases with further displacement as shown in Figs. 15. The crack propagation process of the experiment is not described by Li et al. [30]. Still, this type of crack distribution is predicted for a similar short shear beam test for other models described in [14] and [31].

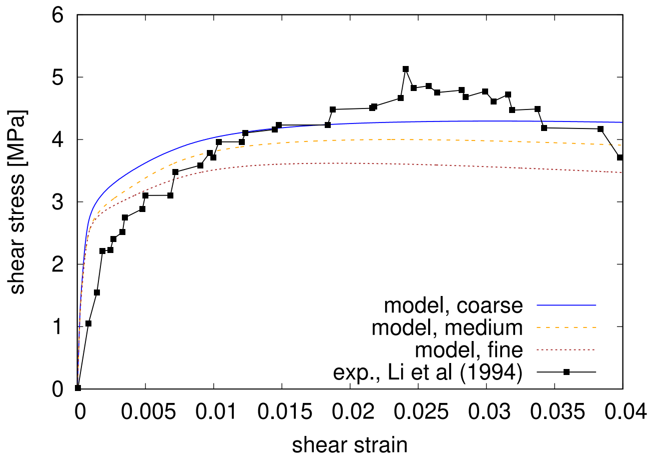

Fig. 13. Model shear strain-shear stress curve of different mesh size compared with experiment. The experimental results are from [30].

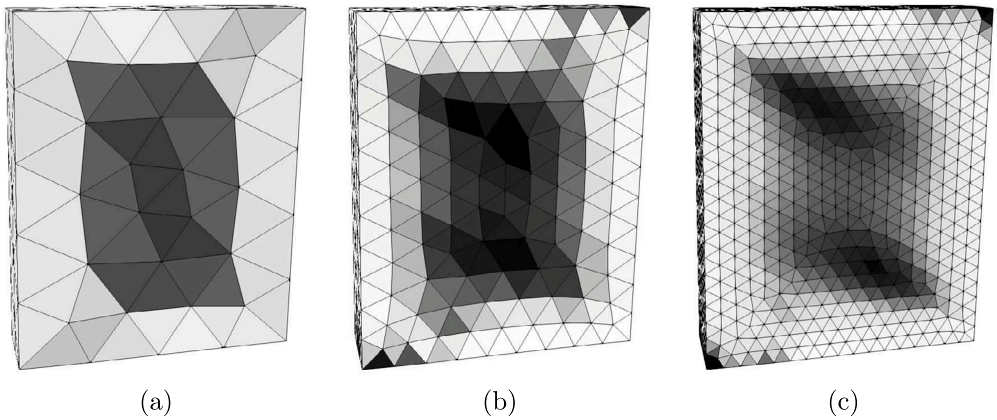

Fig. 14. Contour plot of maximum component of principle strain at an average shear strain of 0.025: (a) mesh size 4 cm, (b) mesh size 2 m, (c) mesh size 1 cm. Here, the colour black corresponds to a threshold of 0.02.

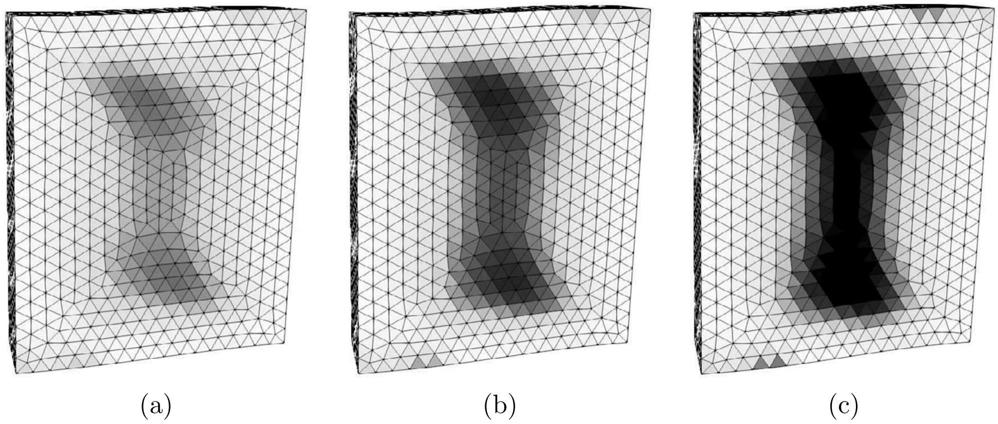

Fig. 15. Contour plot of maximum component of principle strain at an average shear strain of: (a) 0.05, (b) 0.06, (c) 0.07. Here, the colour black corresponds to a strain threshold of 0.06.

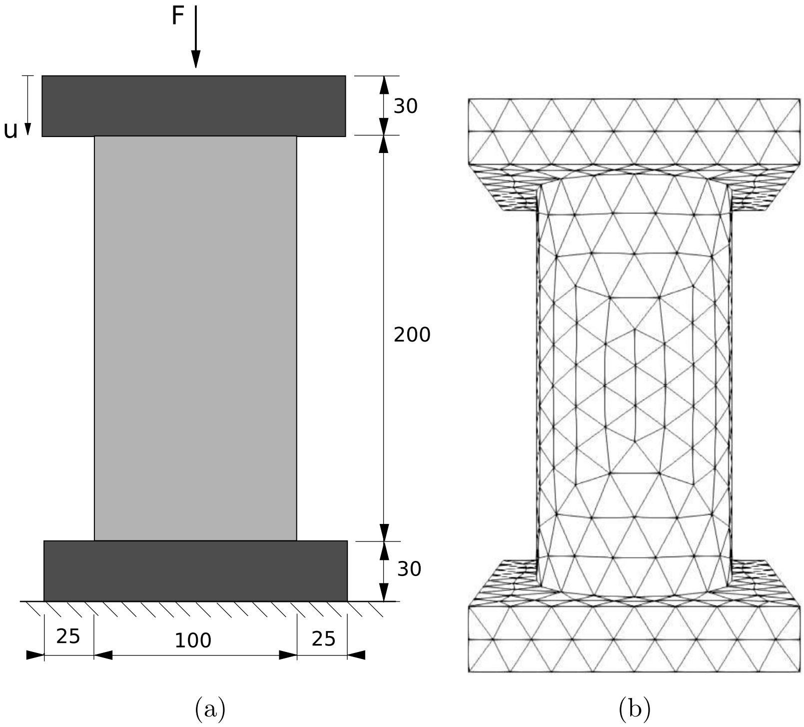

Fig. 16. (a) Compression test geometry and loading setup based on experiments reported in [32] and (b) FE mesh with element size 2 cm.

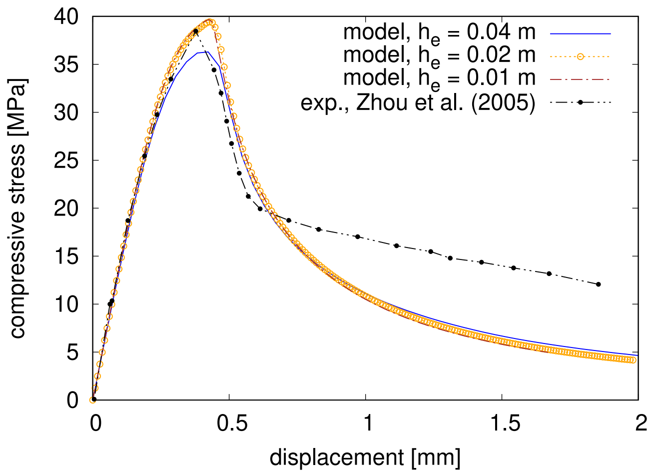

Fig. 17. Stress–displacement curves for different mesh sizes of the structural model compared to experimental result. The experimental results are reported in [32].

6.3. Compression

The last example is a compression test of an ECC cylinder tested in [32]. The geometry and loading setup is shown in Fig. 16a. The ECC specimen is loaded at the top and bottom by means of aluminium plates. The three-dimensional finite element mesh shown in Fig. 16 consists of tetrahedral constant strain elements which were generated with the mesh generator T3D [29]. Meshes of loading plates and specimen are conform. Therefore, there is no slip between specimen and loading plates. Three element mesh sizes were used with element size $h_e = 4$, 2 and 1 cm to investigate the effect of mesh size on the results. This test differs from the tension and shear test, because the compressive response of CDPM2F is not affected by the bridging law that we introduced in the previous sections, so that for pure compression the response of CDPM2F is equal to the response of CDPM2. Therefore, we state here only the input parameters of the matrix. For the ECC cylinder, the input parameters are chosen as matrix Young's modulus $E_m = 30$ GPa,

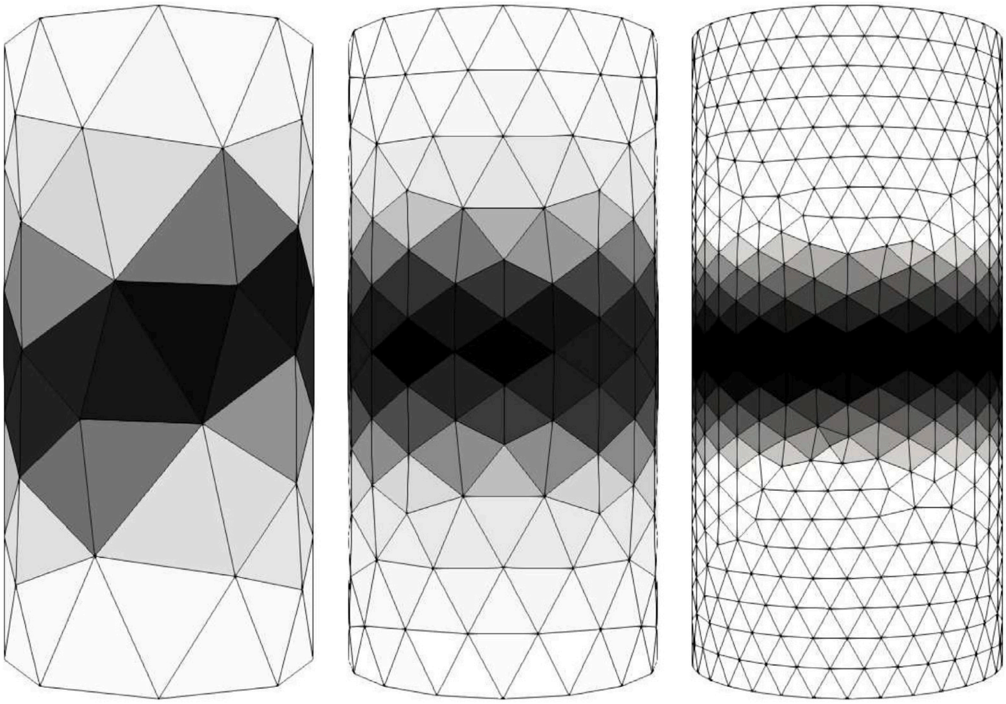

Fig. 18. Influence of mesh size on zz component of strain tensor contour plot of compression tests at displacement 0.6 mm: (a) mesh size 0.04 m, (b) mesh size 0.02 m, (c) mesh size 0.01 m.

Poisson's ratio $\nu = 0.2$, matrix tensile strength $f_c = 2.2$ MPa, matrix compressive strength $f_c = 39.28$ MPa and matrix softening strain threshold for compression as $\varepsilon_f = 0.00001$. For the aluminium plates at the top and bottom of the specimen an elastic constitutive model is used with Young's modulus $E = 70$ GPa and Poisson's ratio $\nu = 0.2$. The stress–displacement curves of the finite element model with different element sizes are compared with the experimental results from in Fig. 17.

Stress–displacement curves of models with different mesh sizes are agree well with experimental results. An almost mesh-independent response is observed. Contour plots of the vertical strain ε_{zz} for the three meshes are shown in Fig. 18 for a vertical displacement of 0.6 mm (see Fig. 17) for the three meshes. The model predicts distributed strains which are greatest in the middle of the specimen, because the edges are restrained by the loading platen.

7. Conclusion

A new plastic-damage approach CDPM2F was developed for the mechanical response of ECC which combines a well accepted fibre law in [11] with the concrete damage plasticity approach CDPM2 [20]. The main conclusions are that

- the model is capable of linking fibre properties to composite response.
- dispersion of fibres is successfully incorporated by the parameter α, which represents the degree of variation of the spatial fibre distribution.
- the model is able to reproduce three-dimensional structural behaviour of components made of ECC.
- the model produces results in both tension, compression and shear which do not exhibit pathological mesh-dependence.

Future work will focus on using the model for structural analysis of steel reinforced members for which the matrix is made of ECC.

CRediT authorship contribution statement

Chao Zhou: Writing – review & editing, Writing – original draft, Visualization, Software, Investigation. **Antoine Marlot:** Writing – review & editing, Investigation. **Peter Grassl:** Writing – review & editing, Writing – original draft, Visualization, Supervision, Software, Formal analysis.

Declaration of competing interest

The authors declare that they have no known competing financial interests or personal relationships that could have appeared to influence the work reported in this paper.

Data availability

Data will be made available on request.

Acknowledgements

The simulations were carried out with the finite element program OOFEM [27] modified by the authors. The finite element meshes were generated with the 3D mesh generator T3D [29]. The finite element code is available at https://github.com/githubgrasp/oofem/releases/tag/cdpm2f-paper. The input files for the analyses can be accessed at https://github.com/githubgrasp/dataCDPM2F/releases/tag/filesForcdpm2fPaper.

References

[1] Naaman AE, Reinhardt HW. Characterization of high performance fiber reinforced cement composites—HPFRCC. In: High performance fiber reinforced cement composites, vol. 2, 1996, p. 1–24.
[2] Zijl GPAGV, Wittmann FH. Durability of strain-hardening fibre-reinforced cement-based composites (SHCC), vol. 4, Springer Science & Business Media; 2010.
[3] Li VC. Engineered cementitious composites (ECC): Bendable concrete for sustainable and resilient infrastructure. Springer; 2019.
[4] Naaman AE, Namur GG, Alwan JM, Najm HS. Fiber pullout and bond slip. I: Analytical study. J Struct Eng 1991;117(9):2769–90.
[5] Redon C, Li V, Wu C, Hoshiro H, Saito T, Ogawa A. Measuring and modifying interface properties of PVA fibers in ECC matrix. J Mater Civ Eng 2001;13(6):399–406.
[6] Marshall DB, Cox BN. A J-integral method for calculating steady-state matrix cracking stresses in composites. Mech Mater 1988;7(2):127–33.
[7] Li VC, Wang SX, Wu C. Tensile strain-hardening behavior or polyvinyl alcohol engineered cementitious composite (PVA-ECC). ACI Mater J 2001;98(6):483–92.
[8] Yang EH, Wang S, Yang Y, Li VC. Fiber-bridging constitutive law of engineered cementitious composites. J Adv Concr Technol 2008.
[9] Moreno DM, Trono W, Jen G, Ostertag C, Billington SL. Tension stiffening in reinforced high performance fiber reinforced cement-based composites. Cem Concr Compos 2014;50:36–46.
[10] Bao G, Song Y. Crack bridging models for fiber composites with slip-dependent interfaces. J Mech Phys Solids 1993;41(9):1425–44.
[11] Lin Z, Li VC. Crack bridging in fiber reinforced cementitious composites with slip-hardening interfaces. J Mech Phys Solids 1997;45(5):763–87.
[12] Yang E-H, Wang S, Yang Y, Li VC. Fiber-bridging constitutive law of engineered cementitious composites. J Adv Concr Technol 2008;6(1):181–93.
[13] Huang T, Zhang YX, Su C, Lo SR. Effect of slip-hardening interface behavior on fiber rupture and crack bridging in fiber-reinforced cementitious composites. J Eng Mech 2015;141(10):04015035.
[14] Kabele P. Assessment of structural performance of engineered cementitious composites by computer simulation, vol. 5.2001, (no. 4). Czech Technical University; 2000.
[15] Kabele P. Multiscale framework for modeling of fracture in high performance fiber reinforced cementitious composites. Eng Fract Mech 2007;74(1–2):194–209.
[16] Liu YM, Bao Y, Deng L, Zhang QH. Experimental and finite element investigations on shear behaviors of stud connectors embedded in engineered cementitious composite (ECC). Eng Struct 2023;277:115438.
[17] Pan ZF, Qiao Z, Si DDS, Shang JQ. Experimental investigation and numerical simulation on uniaxial tensile behavior of hybrid PVA–ECC. Constr Build Mater 2023;398:132517.
[18] Kunieda M, Kozawa K, Ueda N, Nakamura H. Fracture analysis of strain hardening cementitious composites by means of discrete modeling of short fibers. In: FraMCos-8: Proceedings of the 8th international conference on fracture mechanics of concrete and concrete structures. 2010, p. 501–8.
[19] Kang J, Bolander JE. Multiscale modeling of strain-hardening cementitious composites. Mech Res Commun 2016;78:47–54, Recent Advances in Multiscale, Multifunctional and Functionally Graded Materials.
[20] Grassl P, Xenos D, Nyström U, Rempling R, Gylltoft K. CDPM2: A damage-plasticity approach to modelling the failure of concrete. Int J Solids Struct 2013;50(24):3805–16.
[21] Bažant ZP, Nguyen HT, Dönmez AA. Critical comparison of phase-field, peridynamics and crack band model M7 in light of gap test and classical fracture tests. J Appl Mech 2022;1–79.
[22] Bažant ZP, Nguyen HT. Proposal of m-index for rating fracture and damage models by their ability to represent a set of distinctive experiments. J Eng Mech 2023;149(8):04023047.
[23] Bažant ZP, Oh B-H. Crack band theory for fracture of concrete. Mater Struct 1983;16:155–77.
[24] Grassl P, Rempling R. Influence of volumetric-deviatoric coupling on crack prediction in concrete fracture tests. Eng Fract Mech 2007;74:1683–93.
[25] Li M, Li VC. Rheology, fiber dispersion, and robust properties of engineered cementitious composites. Mater Struct 2013;46:405–20.
[26] Zhou J, Qian S, Ye G, Copuroglu O, Van Breugel K, Li VC. Improved fiber distribution and mechanical properties of engineered cementitious composites by adjusting the mixing sequence. Cem Concr Compos 2012;34(3):342–8.
[27] Patzák B. OOFEM – An object-oriented simulation tool for advanced modeling of materials and structure. Acta Polytech 2012;52:59–66.
[28] Kanda T, Li VC. Practical design criteria for saturated pseudo strain hardening behavior in ECC. J Adv Concrete Technol 2006;4(1):59–72.
[29] Rypl D. Sequential and parallel generation of unstructured 3D meshes [Ph.D. thesis], Prague, Czech Republic: Czech Technical University; 1998.
[30] Li V, Mishra DK, Naaman AE, Wight JK, LaFave JM, Wu H-C, et al. On the shear behavior of engineered cementitious composites. Adv Cem Based Mater 1994.
[31] Kanda T, Lin Z, Li VC. Application of pseudo strain-hardening cementitious composites to shear resistant structural elements. In: Proceedings of the 10th international conference on fracture mechanics of concrete and concrete structure (FraMCoS 3), Gifu, Japan. 1998, p. 24–6.
[32] Zhou J, Pan J, Leung CKY. Mechanical behavior of fiber-reinforced engineered cementitious composites in uniaxial compression. J Mater Civ Eng 2014;27(1):04014111.